

# Geometry-sensitive protrusion growth directs confined cell migration

Johannes Flommersfeld,<sup>1,2</sup> Stefan Stöberl,<sup>3</sup> Omar Shah,<sup>1</sup> Joachim O. Rädler,<sup>3</sup> and Chase P. Broedersz<sup>1,2,\*</sup>

<sup>1</sup>*Department of Physics and Astronomy, Vrije Universiteit Amsterdam, 1081HV Amsterdam, Netherlands*

<sup>2</sup>*Arnold Sommerfeld Center for Theoretical Physics and Center for NanoScience, Department of Physics, Ludwig-Maximilian-University Munich, Theresienstraße 37, D-80333 Munich, Germany*

<sup>3</sup>*Faculty of Physics and Center for NanoScience, Ludwig-Maximilian-University, Geschwister-Scholl-Platz 1, D-80539 Munich, Germany*

(Dated: August 17, 2023)

The migratory dynamics of cells can be influenced by the complex micro-environment through which they move. It remains unclear how the motility machinery of confined cells responds and adapts to their micro-environment. Here, we propose a biophysical mechanism for a geometry-dependent coupling between the front of the cell and the nucleus that leads to directed migration. We apply our model to geometry-guided cell migration to obtain insights into the origin of directed migration on asymmetric adhesive micro-patterns and the polarization enhancement of cells observed under strong confinement. Remarkably, for cells that can choose between channels of different size, our model predicts an intricate dependence for cellular decision making as a function of the two channel widths, which we confirm experimentally.

Cell migration underlies several major physiological processes, such as tissue development [1, 2], cancer metastasis [3], and wound healing [4]. During mesenchymal migration, cells rely on the expansion and contraction of protrusions to explore the micro-environment through which they migrate [5, 6]. The expansion of protrusions in the cell membrane is driven by the polymerization of actin, while contraction forces are generated by the interaction between the motor protein myosin II and actin filaments. This protrusion-driven process is used, for example, by invading cancer cells to squeeze through tight pores in the extracellular matrix [5] or to guide the growth of neurons [7] and new blood vessels [8] inside structured tissue. However, biophysically it is still unclear how protrusion-based exploration is influenced by physical cues, such as the geometry or the adhesive properties of the local micro-environment, posing a challenge to understand confined cell migration.

To reduce complexity, several experimental assays were established that focus on specific aspects of physically guided cell migration. These include micro-patterning techniques [9, 10] such as homogeneously coated narrow lanes [11, 12], as well as unisotropic substrates where migration is guided by physical cues such as surface topography [13–15], confinement [16–18], and directed surface patterning [19–22]. While the migration behavior observed on isotropic surfaces can be understood in terms of detailed microscopic models that account for underlying molecular processes [23–27], the migration on unisotropic and confining environments has mostly been studied using phenomenological and data-driven models that are largely agnostic to the underlying molecular and biophysical processes [18–20]. To understand confined cell migration from basic biophysical principles, a mechanistic model is needed that describes the effects of physical cues such as substrate geometry on protrusion growth and how this directs cellular decision making.

Here, we construct a mechanistic model for geometry-sensitive protrusion growth and force generation that describes how cells migrate on simple confining substrates. The key aspect of our model is that the growth of protrusions that direct cell movement is sensitive to the physical properties of the confining substrate, such as adhesiveness or geometry. We demonstrate and test our model by investigating how cell migration is guided by various physical cues in frequently employed experimental assays. To show that our model is applicable to unisotropic environments, we consider "ratchet-like" adhesive patterns. The migration bias predicted by our model describes previous experiments [20, 22]. Subsequently, we consider a second central aspect of physiological cell migration: lateral confinement, where our model provides mechanistic insight into the previously observed stimulation of protrusion growth through lateral confinement [18, 28]. Finally, we illustrate the generalizability of our model by showing that it correctly describes the impact of protrusion confinement on cellular decision making, which we explore experimentally using cells on micro-patterns.

As a starting point, we build on previously developed models for one-dimensional mesenchymal migration of cells that can form protrusions on both sides of the nucleus [25–27]. These models account for actin polymerization against a membrane of surface tension  $\tau$  with a polymerization rate  $r_p$  at both sides of the cell (Fig. 1A). This induces a retrograde flow with velocity  $v_r$  of actin towards the center of the cell. This flow is opposed by so-called focal adhesions, which mechanically connect actin filaments across the membrane to the substrate. These adhesions are typically modeled as elastic bonds that stochastically bind to actin filaments, resulting in a friction force opposing the retrograde flow [27]. To account for the observed coupling between retrograde flow velocity and cell polarity [11], the retrograde flow is assumed to advect a generic polarity cue. The local concentration

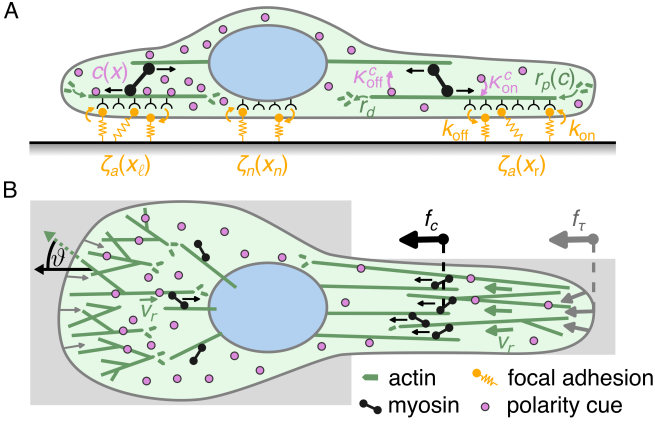


Figure 1. **Components of the migration model.** **A.** Side view showing the key molecular components of the model. **B.** Top view of a cell on an unisotropic substrate. Confinement-induced actin alignment stimulates protrusion growth, resulting in increased membrane tension and retrograde flow.

of this cue controls actin polymerization rates [25, 26]. Protrusion growth is opposed by myosin contractility and membrane tension. In previous work the resulting restoring force was modeled in terms of the effective (visco-)elastic material properties of the cell, which were assumed to be independent of the environment [26, 27]. Hence, the migration dynamics predicted by these models, do not couple to the physical micro-environment of the cell, which restricts their applicability to the case of migration on homogeneous substrates.

To broaden the scope of such models, we note that the geometry and adhesiveness of the environment can determine the shape of the protrusions during migration. To understand how structured substrates impact cell migration, we thus derive the force produced by protrusions as a function of their dimensions. We first consider the force balance at the front of a protrusion, where the actin retrograde flow velocity,  $v_r = \zeta_a^{-1}(f_c + f_\tau)$ , is assumed to be driven by the sum of the myosin generated contractile force  $f_c$  and the membrane force  $f_\tau$  (Fig. 1B), and  $\zeta_a$  is the effective friction coefficient associated to the actin filaments [29]. Myosin motors generate a contractile force by traversing counter-oriented actin filaments inside a network in the crossover region between the protrusion and the cell body, where actin filaments associated with the nucleus and the protrusion overlap [30]. The generated contractile force is, in general, governed by the myosin force-velocity relation [31]. In our case, the myosin velocity is set by  $v_r$ . Since typical nuclear velocities observed in mesenchymal cell migration ( $< 30\text{nm/s}$  [12, 16, 32]) are at least an order of magnitude below the unloaded velocity of myosin motors ( $200 - 800\text{nm/s}$  [33]), we approximate the force generated by a myosin motor by the stall force  $f_s$ . The total number of actin filaments of diameter  $\ell_a$  extending from

the protrusion with width  $w_p$  is set by  $w_p v_r / (r_d \ell_a^2)$ , a balance between the influx due to retrograde flow and the loss due to depolymerization with rate  $r_d$  (see [29]). The myosin number contributing to contractility is then  $w_p v_r / (r_d \ell_a^2) r_m \rho_m$ , where  $r_m$  is an interaction radius and  $\rho_m$  is the myosin line density. Together with the force balance driving retrograde flow, we obtain

$$f_c = \frac{w_p r_m \rho_m f_s}{\ell_a^2 r_d} v_r = \ell_a^{-2} \frac{w_p r_m \rho_m f_s}{\zeta_a r_d - w_p r_m \rho_m f_s} f_\tau. \quad (1)$$

Physically, larger membrane forces increase retrograde flow. This results in a higher actin density in the crossover region and consequently an increased myosin driven contractility (Fig. 1B), which leads to a coupling between myosin contractility and the membrane force.

To obtain an expression for the membrane tension  $f_\tau$ , we consider the formation of a protrusion of length  $L_p$ , height  $h_p$ , and width  $w_p \gg h_p$  [34, 35], which may be constrained by the confining micro-environment. The resulting increase in surface area is opposed by the membrane force  $f_\tau = 2(h_p + w_p)\tau \approx 2w_p\tau$ . Note, for a constant surface tension  $\tau$  the contractile force in Eq. (1) would be independent of the protrusion length, which is incompatible with protrusion-guided migration. However, the surface tension of the cell can vary with a change in surface area [36–38]. We account for this up to linear order, by  $\tau = \tau_0 + 2\tau_1 L_p / h_p$ , with parameters  $\tau_0$  and  $\tau_1$ . The membrane force is then given by

$$f_\tau = 2w_p\tau_0 + \frac{4\tau_1}{h_p} w_p L_p. \quad (2)$$

The first term is due to the baseline tension of the membrane, which should be balanced by the internal pressure of the cytosol, such that only the second term contributes to the mechanical coupling between the nucleus and the protrusion in terms of the contractile force (see Eq. (1))

$$f_c = \frac{4\tau_1 w_p r_m \rho_m f_s}{(\zeta_a r_d - w_p r_m \rho_m f_s) h_p \ell_a^2} w_p L_p = k_c L_p. \quad (3)$$

Note, we defined a linear elastic coupling (spring constant  $k_c$ ) between the nucleus and the protrusion, which has been used as a key component of several migration models [18, 26, 27]. In our model, this elastic coupling emerges from the interplay between an increased membrane tension, retrograde flow and myosin contractility.

Next, we combine this result with the polymerization driven motion of the protrusion edges to derive an equation of motion for the protrusion growth on both sides of the cell. Using that the velocity of the front of the protrusions is given by the difference between the projected actin polymerization velocity  $\ell_a S_{\ell/r} r_p(x_{\ell/r})$  and the retrograde flow velocity, we obtain a dynamical equation for the two protrusion positions  $x_{\ell/r}$

$$\dot{x}_{\ell/r} = -\frac{k_{\ell/r}(x_{\ell/r})}{\zeta_a(x_{\ell/r})} (x_{\ell/r} - x_n) \mp \ell_a S_{\ell/r} r_p(x_{\ell/r}), \quad (4)$$

where  $k_{\ell/r}(x_{\ell/r}) = k_c(x_{\ell/r}) + 4\tau_1 w_p(x_{\ell/r})/h_p$  and the order parameter  $S_{\ell/r} = \langle |\cos(\vartheta_{\ell/r})| \rangle$  measures the average orientation of actin filaments in the direction of protrusion growth (Fig. 1B). The friction coefficient  $\zeta_a(x_{\ell/r})$  accounts for the binding dynamics of the focal adhesions [27]. Since cells can form more adhesions on wider or more densely coated patterns,  $\zeta_a$  generally depends on the position of the protrusion on the substrate [29]. Eq. (4) thus illustrates one aspect induced by the confining geometry on protrusion dynamics: while a wider protrusion can produce larger contractile forces (Eq. (3)), it is bound to the substrate through more adhesive bonds. Consequently, on a substrate with a homogeneous adhesiveness,  $k_{\ell/r}/\zeta_a$  is independent of the width of the protrusions and thus identical on both sides of the cell [29].

The dynamics of the nucleus are given by the balance of contraction forces generated by the two protrusions

$$\dot{x}_n = \frac{k_c(x_\ell)}{\zeta_n(x_n)}(x_\ell - x_n) + \frac{k_c(x_r)}{\zeta_n(x_n)}(x_r - x_n). \quad (5)$$

Since the nucleus is indirectly connected to the substrate through focal adhesions, the nuclear friction coefficient  $\zeta_n$  accounts for viscous drag within the cytosol and adhesion-induced stochastic friction (see [29]).

To complete the model, we require an expression for the polymerization rate  $r_p$  (Eq. (4)), which depends on the local concentration of polarity cues in the cytosol [39, 40]. As the cell polarizes, it builds up a gradient in polarity cues. Here, we account for this by considering the concentration of a generic back-polarity cue that accumulates in the rear of a polarized cell and inhibits actin polymerization (Fig. 1). The difference in the average concentration in the two halves of the cell is  $\Delta c = c_r - c_\ell$ , with  $c_{\ell/r}$  representing the concentration to the left/right of the nucleus and the polarity cue binds to and unbinds from actin filaments with rates  $\kappa_{\text{on}}^c$  and  $\kappa_{\text{off}}^c$ , respectively. Following previous work [11], we assume the polarity cue to be advected with the retrograde flow. The advective flux between the two parts of the cell is then given by  $\Delta v_r n_c c_0$ , where  $\Delta v_r = v_r(x_r) - v_r(x_\ell)$ ,  $n_c = \kappa_{\text{off}}^c / (\kappa_{\text{on}}^c + \kappa_{\text{off}}^c)$  is the bound fraction of the polarity cue and  $c_0$  denotes the polarity cue concentration around the cell mid-plane. The polarity cue flux between the two parts of the cell can thus be written as

$$J(x, t) = -(1 - n_c)\tilde{D}\partial_x c(x, t) - \Delta v_r n_c c_0 + \tilde{\sigma}\xi(t), \quad (6)$$

with diffusion constant  $\tilde{D}$ . We assume the polarity to be the dominating source of noise in the migratory dynamics of the cell, and account for this in Eq. (6) by adding Gaussian white noise  $\xi(t)$  of strength  $\tilde{\sigma}$ .

Treating the overall concentration of the polarity cue  $c_0$  in the cell as conserved, we write the concentration in the two parts of the cell as  $c_{\ell/r} = c_0 \mp \Delta c/2$ . The gradient of the concentration profile can then be approximated as  $\partial_x c(x, t) \approx \Delta c/L_c$ , where  $L_c$  is the length of

the cell. The left and right end of the cell are treated as no-flux boundaries, and the dynamics of  $\Delta c$  can then be approximated by [29]

$$\partial_t \Delta c(t) \approx -D\Delta c(t) - \frac{4n_c c_0}{L_c} \Delta v_r(\Delta c) + \frac{4\tilde{\sigma}}{L_c} \xi(t), \quad (7)$$

with  $D = 4(1 - n_c)\tilde{D}L_c^{-2}$ . Importantly, for a protrusion at steady state, the retrograde flow is equal to the projected polymerization velocity (see Eq. (4)). Expanding  $\Delta v_r$  in terms of  $\Delta c$  on both sides of the cell (see [29]), then allows us to derive an equation for the dynamics of the polarity  $P(t) \equiv -P_0\Delta c(t)$  as

$$\dot{P} = -\alpha P - \beta P^3 + \delta(S_r - S_\ell) + \sigma\xi(t), \quad (8)$$

with  $\sigma = 4P_0\tilde{\sigma}L_c^{-1}$ ,  $\alpha = D - 4n_c c_0 L_c^{-1} \ell_a r_1 (S_r + S_\ell)$ ,  $\beta = 4P_0^{-2} n_c c_0 L_c^{-1} \ell_a r_3 (S_r + S_\ell)$ , and  $\delta = 4P_0 n_c c_0 L_c^{-1} \ell_a r_p (c_0)$ . The coefficients  $r_{1/3} > 0$  stem from the leading order expansion of  $\Delta v_r$ . To couple Eq. (8) to Eq. (4), we note that we can relate the polarization rate to the polarity to leading order as  $r_p(t) = r_p(c_0) + r_1 P_0^{-1} P(t)$ . The resulting mechanistic model given by the closed set of equations (4), (5) and (8) describes protrusion driven 1D confined migration behavior of cells in structured micro-environments. To test this model and investigate what new insights it can give into migration on structured substrates, we apply our model to a variety of different experimentally studied migration assays.

*Migration on Directed Patterns.*— Cell migration can be biased due to unisotropic adhesiveness of the micro-environment [20–22]. Experimentally, this is realized through directed, "ratchet-like" adhesive patterns (Fig. 2A), which induce biased migration, a phenomenon known as "ratchetaxis". The direction of this migration bias depends on the geometry of the micro-pattern. To demonstrate how to capture such asymmetry theoretically, we first consider a cell located on a triangular pattern with two symmetric, rectangular neighboring patterns that its protrusions can engage with (Fig. 2A, left). The triangular shape of the pattern allows the cell to form wider protrusions on the blunt end compared to the pointed end of the triangle. The key mechanism of geometry sensing in our model here follows from Eq. (3): Wider protrusions have an increased effective spring constant and thus  $k_c(x_\ell) > k_c(x_r)$ . Since the boundaries of the pattern are not parallel to the direction of migration, we assume  $S_\ell = S_r$ . Hence, the asymmetry of  $k_c$  leads to a higher pulling force on the nucleus in the direction of the wider side of the pattern (—direction) and consequently we find a migration bias towards the —direction (Fig. 2B).

For cells migrating on a periodic triangular pattern (Fig. 2A, center) however, a second mechanism becomes relevant: due to the tapering of the pattern, the protrusion in the —direction overlaps with non-adhesive regions. This reduces the density of adhesion bonds  $\rho_b$  and

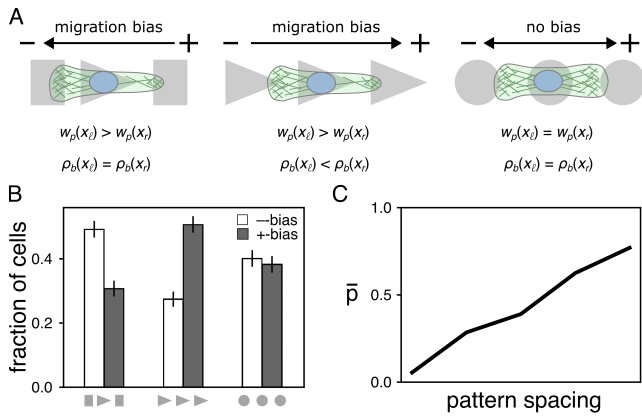


Figure 2. **Modeling cell migration on directed substrates.** **A.** Migration on different directed micro-patterns (ratchetaxis). Triangular patterns lead to protrusions of different protrusion widths  $w_p$  on both sides of the nucleus (left, center) but can also result in different densities of adhesive bonds  $\rho_b$  at the front of the two protrusions (center). **B.** First-step migration biases obtained from simulations of our model on different micro-patterns. **C.** Effect of pattern spacing on the migration bias  $p = (N_+ - N_-)/(N_+ + N_-)$  on periodic patterns, with the number of steps in the  $+/-$ -direction  $N_{+/-}$ .

thus  $k_\ell > k_r$ , resulting in a migration bias in the  $+$ -direction in our simulations (Fig. 2B, Fig. S3 [29]). Bigger gaps between the patterns lead to a stronger asymmetry in the adhesion density below the two protrusions. This reinforces the imbalance between  $k_l$  and  $k_r$  increasing the migration bias (Fig. 2C and S3 [29]). Overall, the predicted migration biases on the different geometries agree well with experimental observations [20, 22].

*Lateral Confinement.*— *In vivo*, cells frequently migrate under conditions of lateral confinement. Experimentally, the effect of confinement is often studied by using micro-patterns [9–11, 41, 42], and this lateral confinement can induce intricate nonlinear migration dynamics [16, 18]. To provide mechanistic insight into these findings, we apply our model to cells migrating through confining channels on adhesive stripes. Actin branching [43] and random fluctuations in the orientations of the actin filaments lead to a range of filament orientations in unconfined cells [30, 44]. We expect the distribution of filament orientations relative to the direction of migration to be narrowed by the confinement (Fig. 3A). This could be either due to direct constraints of the orientations for fibers longer than the width of the pattern or propagation of a preferred orientation over a correlation length scale into the bulk through alignment interactions, as in nematic and polar liquid crystals [45–47].

We account for such boundary-induced alignment by assuming that the order parameter  $S$  increases with increasing confinement of the protrusion as  $S = 1 - sw_p^2$ , where  $s > 0$  is a parameter that accounts for the strength

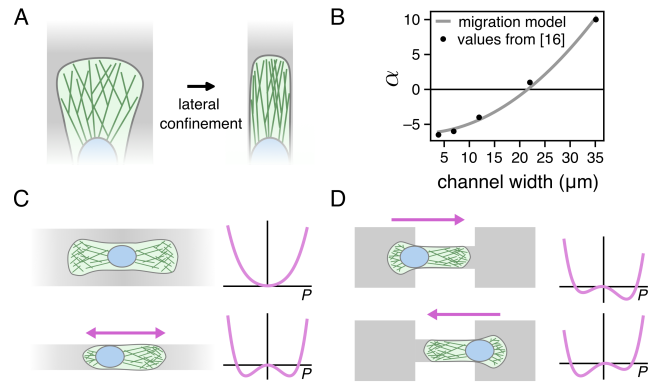


Figure 3. **Modeling cell migration in lateral confinement.** **A.** Lateral confinement of the protrusion leads to alignment of actin filaments. **B.** Fit of the analytical expression for  $\alpha$  on dumbbell-shaped patterns to the values reported in [18]. **C.** and **D.** Lateral confinement induces spontaneous polarization of the cell. For homogeneous confinement (**C.**), both polarization directions are equally likely, while for asymmetric confinement (**D.**), the polarization is biased in the direction of stronger confinement.

of the alignment interactions between actin filaments. This gives us the following expression for  $\alpha$  (see Eq. (8)) as a function of the protrusion width:

$$\alpha(w_{p,\ell}, w_{p,r}) = D - 2n_c c_0 l_a r_1 (2 - sw_{p,r}^2 - sw_{p,\ell}^2). \quad (9)$$

Note, if the protrusions are sufficiently confined,  $\alpha$  becomes negative inducing a self-reinforcement of the polarity and consequently protrusion growth.

The polarity feedback parameter  $\alpha(w_{\text{cell}}, w_c)$  for cells on a pattern wider than the width of the cell  $w_{\text{cell}}$  entering a confining channel of width  $w_c$  with their leading protrusion (see Fig. 1B) is shown in Fig. 3B, and agrees well with a similar inferred model constrained by experimental data [18]. In uniform confinement, both directions of polarization are equally likely, since the bias term in Eq. (8) vanishes (Fig. 3C). However, in a scenario where only one side of the cell is confined (Fig. 3D), our model predicts a bias for the cell to polarize in the direction of the confinement. For migration on dumbbell-shaped micro-patterns we find the same qualitative behavior that was reported in [18] (see [29]) our approach does however present a biophysical mechanism underlying the geometry adaptation of protrusion and polarity dynamics reported there: the sign of  $\alpha(w_{p,\ell}, w_{p,r})$  is set by the competition between advection and diffusion of the polarity cue. Confinement-induced protrusion growth leads to an increase in the advection of the polarity cue towards the rear of the cell. As a consequence, differences in the polarity concentration profile get reinforced under confinement.

Further, our model can be generalized to various other confining geometries, as opposed to prior approaches [18,

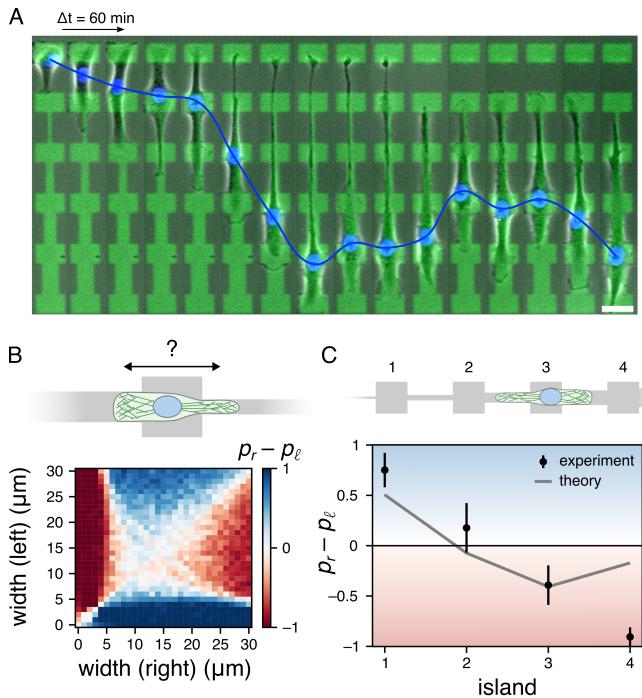


Figure 4. **Cellular decision making in lateral confinement.** **A.** Time series of a cell migrating on a chain of adhesive islands that are connected by adhesive bridges of increasing width (scale bar:  $35\mu\text{m}$ ). **B.** Predicted migration bias for cells encountering different bridge widths on both sides.  $p_{r/\ell}$  denotes the probability that the cell migrates into the right/left channel. **C.** Experimentally observed together with theoretically predicted migration biases.

20, 27]. In particular, our model predicts that confinement can have opposing effects on the preferred direction of migration. On the one hand, confinement-induced actin alignment stimulates polarization in the direction of reduced channel width. On the other hand, the contractile force decreases with stronger confinement (Eq. (3)), leading to a net force on the nucleus away from the confinement. To put this in context, consider a cell that can choose between two channels of different width (Fig. 4B). Interestingly, our model then predicts a non-monotonic dependence of the migration bias on the two bridge widths. To test this prediction, we perform micropattern experiments with cells migrating on a series of square-shaped adhesive islands connected by bridges of increasing width (Fig. 4A) [29]. Our model predicts a transition from a bias towards the wider channels at narrow bridge widths to a bias towards the narrower channel at wider bridge width, which agrees well with the experimentally observed behavior (Fig. 4C). The observed transition in the migration bias yields new insights into the decision making of cells that migrate through confining environments with heterogeneous pore sizes.

To summarize, we developed a generalizable model for directed mesenchymal cell migration in structured micro-

environments from basic biophysical principles. At the core of our model is the coupling between substrate-controlled protrusion formation and cellular migration behavior. Here, it would be insightful to further investigate how the micro-environment affects membrane tension locally and globally. We demonstrated that our model explains the emergence of directed migration in response to different external cues such as asymmetric adhesion densities and the geometry sensing of polarity dynamics [18] in lateral confinement. This model of confined cell migration broadens the scope of cell migration models to more physiological conditions, where cells are simultaneously exposed to different physical migration cues and could form the basis for more complex approaches in the future that also integrate detailed biochemical signaling pathways.

We thank Daniel Riveline, Tom Brandstätter, Janni Harju, David Brückner and Bram Hoogland for helpful discussions. This project was funded by the Deutsche Forschungsgemeinschaft (DFG, German Research Foundation), Project No. 201269156—SFB 1032 (Projects B01 and B12).

\* [c.p.broedersz@vu.nl](mailto:c.p.broedersz@vu.nl)

- [1] C. M. Franz, G. E. Jones, and A. J. Ridley, *Developmental Cell* **2**, 153 (2002).
- [2] C. J. Weijer, *Journal of Cell Science* **122**, 3215 (2009).
- [3] H. Yamaguchi, J. Wyckoff, and J. Condeelis, *Current Opinion in Cell Biology* **17**, 559 (2005).
- [4] W. S. Krawczyk, *Journal of Cell Biology* **49**, 247 (1971).
- [5] P. Friedl and K. Wolf, *Cancer and Metastasis Reviews* **28**, 129 (2009).
- [6] A. J. Ridley, *Cell* **145**, 1012 (2011).
- [7] S. L. Gupton and F. B. Gertler, *Science's STKE* **2007**, 10.1126/stke.4002007re5 (2007).
- [8] H. M. Eilken and R. H. Adams, *Current Opinion in Cell Biology* **22**, 617 (2010).
- [9] R. Singhvi, A. Kumar, G. P. Lopez, G. N. Stephanopoulos, D. I. C. Wang, G. M. Whitesides, and D. E. Ingber, *Science* **264**, 696 (1994).
- [10] C. S. Chen, M. Mrksich, S. Huang, G. M. Whitesides, and D. E. Ingber, *Science* **276**, 1425 (1997).
- [11] P. Maiuri, J.-F. Rupprecht, S. Wieser, V. Rupprecht, O. Bénichou, N. Carpi, M. Coppey, S. De Beco, N. Gov, C.-P. Heisenberg, C. Lage Crespo, F. Lautenschlaeger, M. Le Berre, A.-M. Lennon-Dumenil, M. Raab, H.-R. Thiam, M. Piel, M. Sixt, and R. Voituriez, *Cell* **161**, 374 (2015).
- [12] B. Amiri, J. C. Heyn, C. Schreiber, J. O. Rädler, and M. Falcke, *Biophysical Journal* **122**, 753 (2023).
- [13] A. I. Teixeira, G. A. Abrams, P. J. Bertics, C. J. Murphy, and P. F. Nealey, *Journal of Cell Science* **116**, 1881 (2003).
- [14] D.-H. Kim, K. Han, K. Gupta, K. W. Kwon, K.-Y. Suh, and A. Levchenko, *Biomaterials* **30**, 5433 (2009).
- [15] J. Park, D.-H. Kim, and A. Levchenko, *Biophysical Journal* **114**, 1257 (2018).

- [16] D. B. Brückner, A. Fink, C. Schreiber, P. J. F. Röttgermann, J. O. Rädler, and C. P. Broedersz, *Nature Physics* **15**, 595 (2019).
- [17] A. Pathak and S. Kumar, *Proceedings of the National Academy of Sciences* **109**, 10334 (2012).
- [18] D. B. Brückner, M. Schmitt, A. Fink, G. Ladurner, J. Flommersfeld, N. Arlt, E. Hannezo, J. O. Rädler, and C. P. Broedersz, *Physical Review X* **12**, 031041 (2022).
- [19] J. Comelles, D. Caballero, R. Voituriez, V. Hortigüela, V. Wollrab, A. L. Godeau, J. Samitier, E. Martínez, and D. Riveline, *Biophysical Journal* **107**, 1513 (2014).
- [20] D. Caballero, R. Voituriez, and D. Riveline, *Biophysical Journal* **107**, 34 (2014).
- [21] D. Caballero, J. Comelles, M. Piel, R. Voituriez, and D. Riveline, *Trends in Cell Biology* **25**, 815 (2015).
- [22] S. Lo Vecchio, R. Thiagarajan, D. Caballero, V. Vigon, L. Navoret, R. Voituriez, and D. Riveline, *Cell Systems* **10**, 535 (2020).
- [23] R. J. Hawkins, M. Piel, G. Faure-Andre, A. M. Lennon-Dumenil, J. F. Joanny, J. Prost, and R. Voituriez, *Physical Review Letters* **102**, 058103 (2009).
- [24] P. Recho, T. Putelat, and L. Truskinovsky, *Physical Review Letters* **111**, 108102 (2013).
- [25] I. Lavi, M. Piel, A.-M. Lennon-Duménil, R. Voituriez, and N. S. Gov, *Nature Physics* **12**, 1146 (2016).
- [26] J. E. Ron, P. Monzo, N. C. Gauthier, R. Voituriez, and N. S. Gov, *Physical Review Research* **2**, 033237 (2020).
- [27] P. Sens, *Proceedings of the National Academy of Sciences* **117**, 24670 (2020).
- [28] S. Jain, V. M. L. Cachoux, G. H. N. S. Narayana, S. de Beco, J. D'Alessandro, V. Cellerin, T. Chen, M. L. Heuzé, P. Marcq, R.-M. Mège, A. J. Kabla, C. T. Lim, and B. Ladoux, *Nature Physics* **16**, 802 (2020).
- [29] See Supplemental Material at [URL will be inserted by publisher] for details on the derivation and implementation of the model, the experimental methods as well as the derivation of an approximate model that only accounts for a single protrusion coordinate. The Supplemental Material contains Refs. [48–50].
- [30] T. M. Svitkina, A. B. Verkhovsky, K. M. McQuade, and G. G. Borisy, *Journal of Cell Biology* **139**, 397 (1997).
- [31] J. Howard, in *Mechanics of motor proteins and the cytoskeleton* (Sinauer, 2005) pp. 263–283.
- [32] S. L. Gupton and C. M. Waterman-Storer, *Cell* **125**, 1361 (2006).
- [33] J. Howard, in *Mechanics of motor proteins and the cytoskeleton* (Sinauer, 2005) pp. 213–227.
- [34] V. M. Laurent, S. Kasas, A. Yersin, T. E. Schäffer, S. Catsicas, G. Dietler, A. B. Verkhovsky, and J.-J. Meister, *Biophysical Journal* **89**, 667 (2005).
- [35] R. Shahapure, F. Difato, A. Laio, G. Bisson, E. Ercolini, L. Amin, E. Ferrari, and V. Torre, *Biophysical Journal* **98**, 979 (2010).
- [36] N. C. Gauthier, M. A. Fardin, P. Roca-Cusachs, and M. P. Sheetz, *Proceedings of the National Academy of Sciences* **108**, 14467 (2011).
- [37] A. R. Houk, A. Jilkine, C. O. Mejean, R. Boltysanskiy, E. R. Dufresne, S. B. Angenent, S. J. Altschuler, L. F. Wu, and O. D. Weiner, *Cell* **148**, 175 (2012).
- [38] C. Roffay, G. Molinard, K. Kim, M. Urbanska, V. Andrade, V. Barbarasa, P. Nowak, V. Mercier, J. García-Calvo, S. Matile, R. Loewith, A. Echard, J. Guck, M. Lenz, and A. Roux, *Proceedings of the National Academy of Sciences* **118**, e2103228118 (2021).
- [39] W.-J. Rappel and L. Edelstein-Keshet, *Current Opinion in Systems Biology* **3**, 43 (2017).
- [40] S. Iden and J. G. Collard, *Nature Reviews Molecular Cell Biology* **9**, 846 (2008).
- [41] V. P. Sharma, B. T. Beaty, A. Patsialou, H. Liu, M. Clarke, D. Cox, J. S. Condeelis, and R. J. Eddy, *IntraVital* **1**, 77 (2012).
- [42] C. Schreiber, B. Amiri, J. C. J. Heyn, J. O. Rädler, and M. Falcke, *Proceedings of the National Academy of Sciences* **118**, e2009959118 (2021).
- [43] R. D. Mullins, J. A. Heuser, and T. D. Pollard, *Proceedings of the National Academy of Sciences* **95**, 6181 (1998).
- [44] J. V. Small, M. Herzog, and K. Anderson, *Journal of Cell Biology* **129**, 1275 (1995).
- [45] J. D. Lee and A. C. Eringen, *The Journal of Chemical Physics* **55**, 4509 (1971).
- [46] D. Saintillan and M. J. Shelley, *Comptes Rendus Physique* **14**, 497 (2013).
- [47] S. Fürthauer, B. Lemma, P. J. Foster, S. C. Ems-McClung, C.-H. Yu, C. E. Walczak, Z. Dogic, D. J. Needleman, and M. J. Shelley, *Nature Physics* **15**, 1295 (2019).
- [48] E. A. Evans and D. A. Calderwood, *Science* **316**, 1148 (2007).
- [49] G. I. Bell, *Science* **200**, 618 (1978).
- [50] J. Damiano-Guercio, L. Kurzawa, J. Mueller, G. Dimchev, M. Schaks, M. Nemethova, T. Pokrant, S. Brühmann, J. Linkner, L. Blanchoin, M. Sixt, K. Rottnert, and J. Faix, *eLife* **9**, e55351 (2020).

# Geometry-sensitive protrusion growth directs confined cell migration

Johannes Flommersfeld,<sup>1,2</sup> Stefan Stöberl,<sup>3</sup> Omar Shah,<sup>1</sup> Joachim O. Rädler,<sup>3</sup> and Chase P. Broedersz<sup>1,2,\*</sup>

<sup>1</sup>*Department of Physics and Astronomy, Vrije Universiteit Amsterdam, 1081HV Amsterdam, Netherlands*

<sup>2</sup>*Arnold Sommerfeld Center for Theoretical Physics and Center for NanoScience, Department of Physics, Ludwig-Maximilian-University Munich, Theresienstraße 37, D-80333 Munich, Germany*

<sup>3</sup>*Faculty of Physics and Center for NanoScience, Ludwig-Maximilian-University, Geschwister-Scholl-Platz 1, D-80539 Munich, Germany*

## DETAILS OF THE MODEL DERIVATION AND IMPLEMENTATION

### Internal and stochastic friction

We consider the friction forces that act on the protrusions and the nucleus. There are two contributions to this friction: internal friction due to the interaction of actin filaments/the nucleus with the cytosol and stochastic friction due to the binding and unbinding dynamics of the focal adhesions. We first consider the friction forces acting on the actin filaments at the front of the protrusion  $x_f$ . The total force exerted by the adhesion bonds is given by  $f_{\text{ad}} = \rho_b \langle n f_b \rangle \ell_r w_p$ , where  $\rho_b$  is the total surface density of bonds,  $n$  is the fraction of bound bonds,  $f_b$  is the force per bond,  $w_p$  is the width of the protrusion and  $\ell_r$  is the region at the front of the protrusion over which the retrograde flow is concentrated. When approximating  $\langle n f_b \rangle \approx n \langle f_b \rangle$ , one can express the total force exerted by bound adhesion bonds in terms of the retrograde flow as [1]

$$f_{\text{ad}} = \zeta_1^a(f_b) v_r \quad (\text{S1})$$

with

$$\zeta_1^a(f_b) = \frac{\rho_b \ell_r k_b n(f_b) w_p}{k_{\text{off}}(f_b)}. \quad (\text{S2})$$

Since the binding and unbinding dynamics of the bonds can be mechanosensitive,  $\zeta_1^a$  will in general depend on the force per bond  $f_b$ . Overall, we see that the collective binding and unbinding dynamics of the adhesion bonds lead to a friction force acting on the F-actin in the protrusion.

Additional to this stochastic friction, there is also internal friction that the actin filaments experience as they move through the cytosol. We write this internal friction as  $f_i^a = \zeta_0^a v_r$ , where  $\zeta_0^a$  is the internal friction coefficient of actin filaments. Taken together we get the following expression for the total friction force:

$$f_f^a = (\zeta_0^a + \zeta_1^a(f_b)) v_r, \quad (\text{S3})$$

Analogously, a similar friction force acts on the nucleus, which we write as

$$f_f^n = (\zeta_0^n + \zeta_1^n(f_b)) v_n. \quad (\text{S4})$$

Here, we replaced the retrograde flow with the nuclear velocity  $v_n$  and  $\zeta_1^n(f_b) = \rho_b \ell_n k_b n(f_b) w_n / k_{\text{off}}(f_b)$ , where  $\ell_n$  and  $w_n$  denote the length and the width over which the nucleus is mechanically interacting with focal adhesions.

In the case of purely surface-confined cell migration, it was found that it is not necessary to account for the mechanosensitivity of the adhesion bonds to explain the observed migration behavior [1, 2]. Hence, we assume that the load per adhesion bond  $|f_b|$  is negligible compared the characteristic molecular force scale  $f_b^*$  [3, 4] and thus  $n = n_0$  and  $k_{\text{off}} = k_{\text{off}}^0$ . Furthermore, for the friction acting on the front of the cell, we expect the focal adhesions to be the main contribution to the total friction due to the importance of focal adhesions for the formation of intact lamellipodia [5]. Consequently, we can write the total friction acting on the front of the cells as

$$f_f^a \approx \zeta_1^a(0) v_r = \zeta_a v_r, \quad (\text{S5})$$

where we defined  $\zeta_a = \zeta_1^a(0) = \rho_b \ell_r k_b n_0 w_p / k_{\text{off}}^0$ .

In contrast, since the nucleus is much larger than the actin filaments, it is less clear if the internal friction can be neglected. Hence, we keep both sources of friction in that case and get

$$f_f^n = (\zeta_0^n + \zeta_1^n(0)) v_n = \zeta_n v_n. \quad (\text{S6})$$

### Actin density in the crossover region

In the crossover region between the protrusion and the nucleus, new filamentous actin is transported in with a rate  $v_r/\ell_a$ , where  $\ell_a$  denotes the size of an actin monomer. Towards the nucleus, we expect the retrograde flow to cease such that the main contribution to the loss of filamentous actin in that region is actin depolymerization with a constant rate  $r_p$ . The number of actin filaments  $N_F$  in the crossover region is then given by

$$\dot{N}_F(t) = \frac{v_r w_p}{\ell_a^2} - r_d N_F(t). \quad (\text{S7})$$

At steady state we thus get

$$N_F(v_r) = \frac{v_r w_p}{r_d \ell_a^2}. \quad (\text{S8})$$

In the crossover region, myosin links actin strands of opposite orientations to form contractile units that ultimately generate the contraction forces acting on the focal adhesions [6]. The number of myosin motors that can interact with an actin filament are given by  $r_m \rho_m$ , where  $r_m$  denotes the myosin interaction radius and  $\rho_m$  is the myosin line density. Thus, the number of contractile actomyosin configurations  $N_{\text{am}}$  is then given by

$$N_{\text{am}} = r_m \rho_m N_F(v_r) = \frac{w_p r_m \rho_m}{\ell_a^2 r_d} v_r, \quad (\text{S9})$$

Multiplying Eq. (S9) by the stall force of a single myosin filament  $f_s$  leads to Eq. (1) in the main text.

### Approximation of the advection-diffusion equation with no-flux boundaries

Starting from Eq. (6) in the main text, we approximate  $\partial_x c \approx \Delta c/L_c$ . From this, we get

$$J(\Delta c, t) \approx -(1 - n_c) \tilde{D} L_c^{-1} \Delta c - n_c c_0 \Delta v_r + \tilde{\sigma} \xi(t). \quad (\text{S10})$$

The local change in concentration of the polarity cue is given by

$$\frac{\partial c(x, t)}{\partial t} = -\frac{\partial J(x, t)}{\partial x}. \quad (\text{S11})$$

In principle Eq. (S11) describes the concentration profile along the entire long axis of the cell. We are, however, only interested in the average difference between the side edges of the cell. We treat the membrane as a no-flux boundary, such that the only flux of polarity cue in or out of the two halves of the cell is through the midplane. Discretizing the gradient of the flux for each half of the cell then gives

$$\frac{\partial c_r(t)}{\partial t} \approx -\frac{0 - J}{L_c/2} = 2L_c^{-1} J \quad (\text{S12})$$

and

$$\frac{\partial c_\ell(t)}{\partial t} \approx -\frac{J - 0}{L_c/2} = -2L_c^{-1} J. \quad (\text{S13})$$

Using  $\Delta c = c_r - c_\ell$ , we then get an approximate expression for the dynamics of  $\Delta c$  in a cell with no-flux boundary conditions

$$\frac{\partial \Delta c}{\partial t} \approx \frac{4J(\Delta c, t)}{L_c}. \quad (\text{S14})$$

Plugging Eq. (S10) into Eq. (S14) then yields Eq. (7) from the main text.

### Expansion of the retrograde flow velocity

To find a simple expression for the difference in retrograde flow velocities  $\Delta v_r(\Delta c) = \ell_a S_r r_p(x_r) - \ell_a S_\ell r_p(x_\ell)$ , we split  $r_p$  in an even ( $r_p'$ ) and an odd ( $r_p''$ ) part in  $\Delta c$ . Together with  $c(x_{\ell/r}) = c_0 \mp \Delta c(t)/2$ , we can then write

$$\Delta v_r(\Delta c) = \ell_a r_p'(\Delta c)(S_r - S_\ell) + \ell_a r_p''(\Delta c)(S_r + S_\ell), \quad (\text{S15})$$

The even term in  $\Delta c$  will enter in Eq. (7) from the main text as a bias term, which dilutes the side of the cell in which the actin filaments are more aligned with the direction of migration. Due to its simple effect as a bias term, we do not expect the detailed functional dependence of  $r_p'$  to be of great effect and thus only keep the leading order term such that  $r_p' \approx r_p'(c_0)$ . The odd term, however, will either dampen or reinforce the concentration gradient depending on its sign. Since we are considering a back-polarity cue, we expect that the odd term leading order has a reinforcing effect on the concentration gradient. To ensure that  $\Delta c$  remains bound, we expand  $r_p''$  up to third order, such that  $r_p''(\Delta c) \approx -r_1 \Delta c + r_3 \Delta c^3$ , with  $r_{1/3} > 0$ . This gives the following approximate expression for  $\Delta v_r$ :

$$\Delta v_r(\Delta c) = \ell_a r_p'(c_0)(S_r - S_\ell) - \ell_a r_1(S_r + S_\ell)\Delta c + \ell_a r_3(S_r + S_\ell)\Delta c^3 \quad (\text{S16})$$

### Effect of ratchet geometry on the model parameters

Here we want to discuss the effects of ratchet-like patterns on the model parameters. As discussed in the main text the ratchet-like geometry has two effects on the protrusions. First, on the wider side ( $--$ -direction), the cell can form wider/more protrusions. Using Eq. (3) from the main text together with Eq. (S5), we find that  $k_c \propto w_p$ . As a consequence, on ratchet patterns, we expect  $k_c(x_\ell) > k_c(x_r)$ . Second, for the protrusion in the  $--$ -direction the fraction of surface area that overlaps with an adhesive region is reduced due to the triangular shape of the patterns (see Fig. 2 in the main text) and thus the density of adhesion bonds  $\rho_b$  is reduced. This affects the friction coefficient  $\zeta_a$  that acts on the protrusion. From Eq. (S5) it follows that  $\zeta_a \propto \rho_b$ , such that we expect  $\zeta_a(x_\ell) < \zeta_a(x_r)$ . Note that in general also  $k_c$  depends on  $\zeta_a$  (Eq. (3) in the main text). This dependence, however, is weaker than the dependence of  $k_\ell/r/\zeta_a$ , such that we neglect it here for simplicity.

To analyze how the geometry affects the migration behavior, we increase both  $k_\ell/\zeta_a$  and  $k_c(x_\ell)/\zeta_n$  while keeping  $k_r/\zeta_a$  and  $k_c(x_r)/\zeta_n$  fixed and calculate the resulting average migration bias (see Fig. S1) for different feedback strengths  $\delta$ . We find that increasing  $k_c(x_\ell)/\zeta_n$  leads to a migration bias in the  $--$ -direction, while additionally increasing  $k_\ell/\zeta_a$  reverses this effect and results in a bias in the  $+$ -direction. The magnitude of  $\delta$  does not change this result qualitatively, but affects the size of the regions with  $+/-$ -bias. Increasing the spacing between consecutive patterns enhances the discrepancy in densities of adhesion bonds between the two protrusion. Hence, we can model this by increasing  $k_\ell/\zeta_a$  while keeping  $k_c(x_\ell)/\zeta_n$  fixed (gray arrow in Fig. S1).

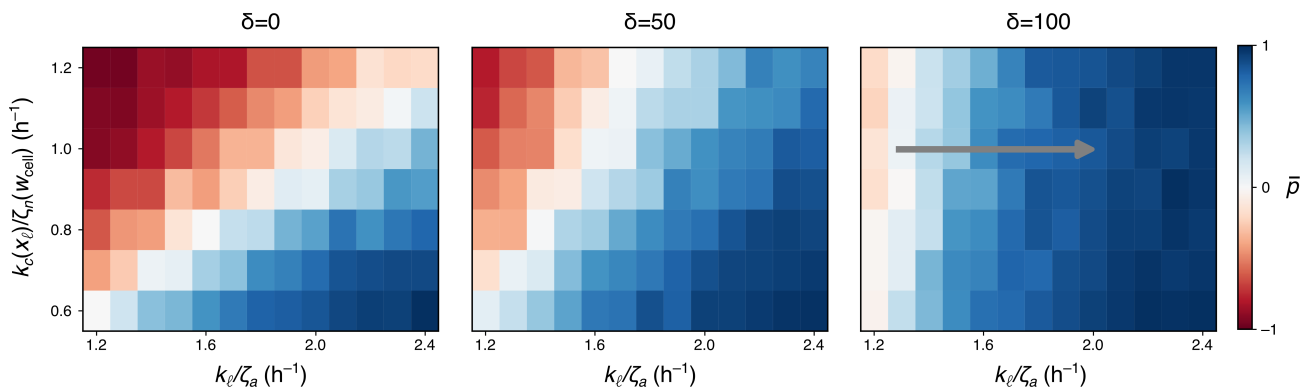


Figure S1. **Migration Biases.** Parameter sweeps of the model with asymmetric protrusions on ratchet-like patterns for different values of  $\delta$ . The gray arrow corresponds to a change in pattern spacing.

### Pattern width dependence of the nuclear friction

In the absence of confinement, the friction that the cell experiences, will be determined by the unconfined width of the cell  $w_{\text{cell}}$ , such that  $\zeta_n(x_n) = \zeta_n(w_{\text{cell}})$ . As the cell migrates into a constriction of width  $w_c$  that is narrower than the width of the cell, the friction coefficient will gradually decrease until the entire nuclear region is confined to the width  $w_c$ . To isolate the effect of the confinement, we rewrite the nuclear friction coefficient as  $\zeta_n(x_n) = \gamma(x_n)\zeta_n(w_{\text{cell}})$ , with  $\gamma(x_n) = \zeta_n(x_n)/\zeta_n(w_{\text{cell}})$ .

In general,  $\gamma(x_n)$  is determined by integrating over the entire nuclear region. Here, we either consider patterns with individual or periodic confinements. In that case, we approximate the complicated spacial dependence of  $\gamma(x_n)$  by following our approach from previous work [2] as

$$\gamma(x_n) = \frac{\zeta_n(w_c)}{\zeta_n(w_{\text{cell}})} + \frac{1}{2} \left( 1 - \frac{\zeta_n(w_c)}{\zeta_n(w_{\text{cell}})} \right) \left( 1 - \cos \left( \frac{2\pi(x_n - x_{\text{center}})}{L} \right) \right), \quad (\text{S17})$$

where  $x_{\text{center}}$  denotes the center of the confinement and  $L$  is the period of the pattern. The bridge width dependence of the minimal value of  $\gamma(x_n)$ , which is given by

$$\frac{\zeta_n(w_c)}{\zeta_n(w_{\text{cell}})} = \frac{1 + \rho_b \ell_n k_b n_0 / (k_{\text{off}}^0 \zeta_n^n) w_c}{1 + \rho_b \ell_n k_b n_0 / (k_{\text{off}}^0 \zeta_n^n) w_{\text{cell}}} \quad (\text{S18})$$

is in excellent agreement with the values found in [2] by fitting the experimentally observed nuclear velocities for varying bridge widths (see Fig. S2).

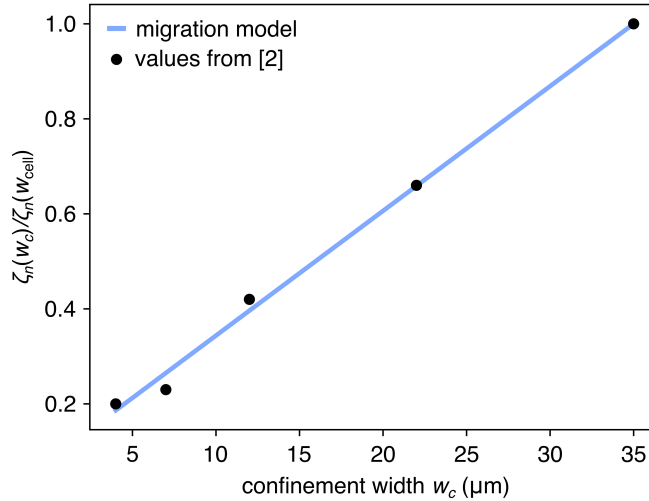


Figure S2. **Nuclear Friction.** Best fit of the minimal value of  $\gamma(x_n)$  given by Eq. (S18) to the values used in [2] that were constrained from experimental data.

### The role of boundary effects

To exclude boundary effects as a possible explanation for the observed switch in preferred migration direction on the chain of islands shown in Fig. 4 in the main text, we simulate our model with symmetric, geometry independent values of  $k_c/\zeta_n$  while keeping everything else identical to the simulations shown in Fig. 4c in the main text. We find the width dependence of  $k_c/\zeta_n$  to be essential to explain the strong bias towards wider channels on island 1 (Fig. S3), indicating is indeed a consequence of the asymmetrically shaped protrusions and not an artifact of the boundaries of the pattern.

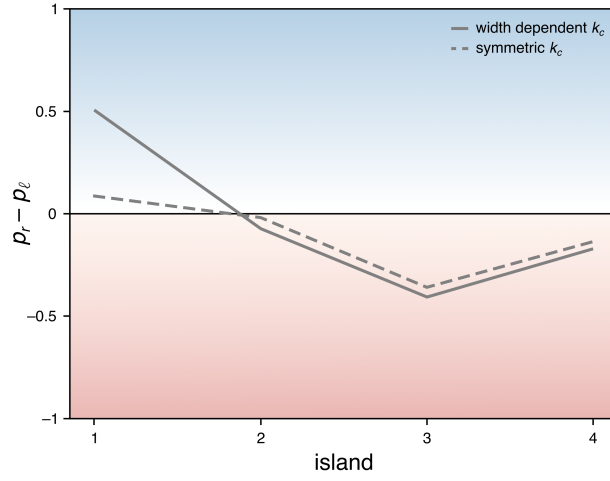


Figure S3. **Importance of the width dependence of  $k_c/\zeta_n$ .** A model with symmetric, geometry-independent values of  $k_c/\zeta_n$  fails to predict the strong bias towards the wider bridge on island 1.

### MODEL PARAMETERS

The used values for the different model parameters are given in Table I.

geometry	single triangle	periodic triangle	periodic circles	dumbbell	island chain
$k_\ell/\zeta_a$ ( $\text{h}^{-1}$ )	1.2	1.4	1.2	1.2	1.2
$k_r/\zeta_a$ ( $\text{h}^{-1}$ )	1.2	1.2	1.2	1.2	1.2
$k_c(x_\ell)/\zeta_n(w_{\text{cell}})$ ( $\text{h}^{-1}$ )	1.0	1.0	0.6	0.6	$0.6 \min(w_p(x_\ell)/10, 1)$
$k_c(x_r)/\zeta_n(w_{\text{cell}})$ ( $\text{h}^{-1}$ )	0.6	0.6	0.6	0.6	$0.6 \min(w_p(x_\ell)/10, 1)$
$\zeta_n(w_c)/\zeta_n(w_{\text{cell}})$	0.2	0.2	0.2	$\frac{1+0.25w_c}{1+0.25\cdot 35\mu\text{m}}$	$\frac{1+0.25w_c}{1+0.25\cdot 35\mu\text{m}}$
$L$ ( $\mu\text{m}$ )	106.5	106.5	106.5	52.5	85
$\ell_a r_p(c_0)$ ( $\mu\text{m h}^{-1}$ )	40	40	40	5	20
$D - 4n_c c_0 L_c^{-1} \ell_a r_1$ ( $\text{h}^{-1}$ )	1.5	1.5	1.5	-22.92	-22.92
$4n_c c_0 L_c^{-1} \ell_a r_1 s$ ( $\mu\text{m}^{-2} \text{h}^{-1}$ )	0	0	0	0.01356	0.01356
$\beta$ ( $\mu\text{m}^{-2} \text{h}$ )	0	0	0	0.001	0.001
$\delta$ ( $\text{h}^{-2}$ )	100	100	100	150	300
$\sigma$ ( $\mu\text{m h}^{-3/2}$ )	100	100	100	100	100
$\ell_a r_1 P_0^{-1}$	1	1	1	1	1

Table I. Model parameters used for the different geometries if not explicitly stated otherwise.

## APPROXIMATE MODEL WITH A SINGLE PROTRUSION COORDINATE

Starting from Eqs. (4) and (5) in the main text, we want to derive from basic biophysical principles a data-driven model we found previously for mesenchymal cell migration inferred from experiments on dumbbell-shaped micro-patterns [2]. This model, however, only considers a single protrusion coordinate

$$x_p = \frac{\Delta x_\ell x_\ell + \Delta x_r x_r}{\Delta x_\ell + \Delta x_r}, \quad (\text{S19})$$

where  $\Delta x_{\ell/r}$  denotes the growth of the respective protrusion between two consecutive experimental observation times spaced by  $\Delta t$ . While  $\Delta x_{\ell/r}$  exhibit an intricate position and time dependence, we can show that we obtain the model found in [2] as an approximation of the more detailed model derived in the main text.

Assuming that the dynamics of  $\Delta x_{\ell/r}$  are slower than the dynamics of  $x_{\ell/r}$ , we can approximate the dynamics of the protrusion coordinate as

$$\dot{x}_p = -\frac{k}{\zeta_a}(x_p - x_n) + \frac{\Delta x_r}{\Delta x_{\text{tot}}}\ell_a S_r T_p(x_r) - \frac{\Delta x_\ell}{\Delta x_{\text{tot}}}\ell_a S_\ell r_p(x_\ell), \quad (\text{S20})$$

where  $k = k_\ell = k_r$  and  $\Delta x_{\text{tot}} = \Delta x_\ell + \Delta x_r$ . Eq. (S20) contains a simple elastic coupling to the nucleus and a complex dependence on the projected polymerization rate in both protrusions. This second part is phenomenologically captured in [2] by introducing a confinement potential that can be interpreted as the outer boundaries of the micro-pattern prohibiting further actin polymerization and a polarization force  $P(t)$  that essentially follows Eq. (8) from the main text. In [2], the values of  $\alpha$  in the center of the channel were determined by fitting the experimentally observed protrusion dynamics for each bridge width, while here we obtain an analytical expression for the bridge width dependence of  $\alpha(x_p)$  in Eq. (9) in the main text. The found expression is consistent with the values obtained from fitting in [2] (see Fig. 3B, main text). The main difference between Eq. (8) in the main text and [2] is the inclusion of a bias term. Both models, however, lead to a qualitatively similar transition behavior (see Fig. S4).

Next, we consider the nuclear dynamics given by Eq. (5) in the main text. Note that we can rewrite the prefactors as

$$\frac{k_c(x_{\ell/r})}{\zeta_n(w_n)} = \frac{k_c(x_{\ell/r})}{\zeta_n(w_{\text{cell}})}\gamma(x_n)^{-1}, \quad (\text{S21})$$

where  $\zeta_n(w_n)$  is given by Eq. (S4) and  $w_{\text{cell}}$  denotes the unconfined width of the cell. The first term in Eq. (S21) can be interpreted as the rescaled spring constant used in [2], while the second term is equivalent to the phenomenological friction coefficient in [2].

Note that the rescaled spring constant in Eq. (S21) depends on the position of the protrusion, while it is assumed to be constant in [2]. However, since the protrusion coordinate strongly fluctuates, it is reasonable to approximate  $k_c(x_{\ell/r}) \approx \langle k_c(x_{\ell/r}) \rangle$ , which can be assumed to be roughly constant. We can then rewrite Eq. (5) of the main text as

$$\dot{x}_n \approx \gamma_n(x_n)^{-1} k_n (x_\ell + x_r - 2x_n), \quad (\text{S22})$$

with

$$k_n = \frac{\langle k_c(x_{\ell/r}) \rangle}{\zeta_n(w_{\text{cell}})}. \quad (\text{S23})$$

In the limiting cases of a strongly polarized cell towards the right  $\Delta x_\ell + \Delta x_r \approx \Delta x_r$ . In that case,  $x_\ell \approx x_n$  and  $x_r \approx x_p$ , such that  $x_\ell + x_r - 2x_n \approx x_p - x_n$ . Similarly, in the case of a completely unpolarized cell,  $\Delta x_r = \Delta x_\ell$  and thus  $x_\ell + x_r = 2x_p$ . At the same time,  $x_p \approx x_n$ , such that again  $x_\ell + x_r - 2x_n \approx x_p - x_n$ . Hence, in those two limiting cases we recover the nuclear dynamics found in [2].

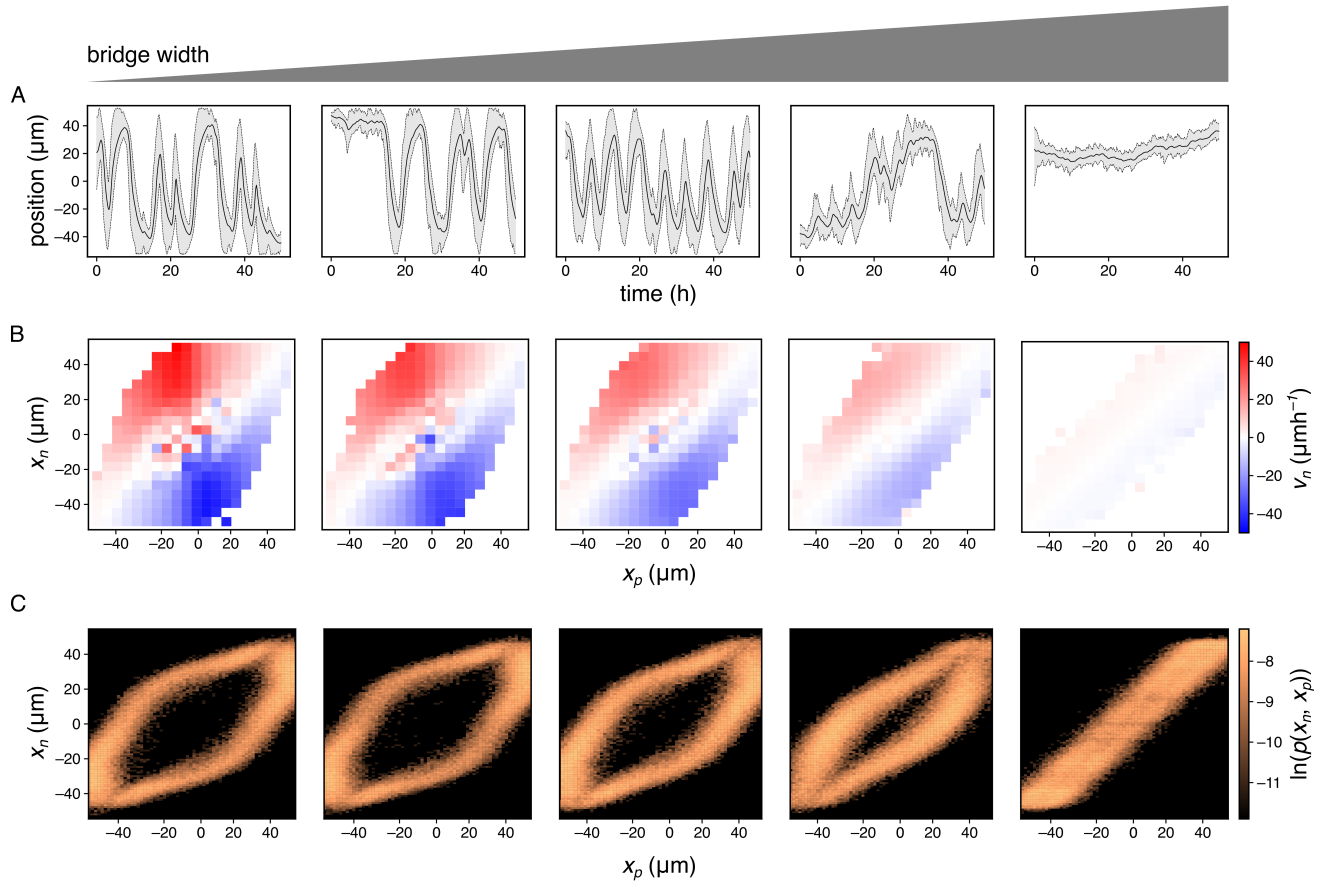


Figure S4. **Dynamics of the two protrusion model for varying bridge widths (4 $\mu\text{m}$ , 7 $\mu\text{m}$ , 12 $\mu\text{m}$ , 22 $\mu\text{m}$  and 35 $\mu\text{m}$ ).** **A.** Example trajectories. **B.** Nuclear velocity maps. **C.** Joint probability density.

## EXPERIMENTAL METHODS

### Micropatterning and sample preparation

To passivate the surface of the ibiTreat  $\mu$ -dish (ibidi), a small drop of 0.01% (w/v) PLL (ThermoFisher) was applied onto the surface of the dish. After incubating the dish at room temperature for a duration of 30min, the PLL-coated dish was rinsed using HEPES buffer (Roche, pH=8.3) to ensure thorough cleansing and preparation. A solution of mPEG-SVA (LaysanBio) with a concentration of 100mg/ml, diluted in 0.1M Hepes, was uniformly distributed onto the PLL-coated dish. The dish was then subjected to an incubation period for at least 1h at room temperature, allowing for appropriate bonding. Following this incubation, the dish was rinsed thoroughly with milliQ water to remove any residual substances. The passivated dish was then photopatterned using the PRIMO module (Alvéole), which was integrated into an automated inverted microscope (Nikon Eclipse Ti). This photopatterning process involved the utilization of the photoactivable reagent PLPP (Alvéole). To ensure uniform distribution of the PLPP gel, it was appropriately diluted in 99% ethanol before being applied onto the passivated surface of the dish. The placement of the dumbbell-chain pattern onto the dish was achieved using the Leonardo software (Alvéole), and subsequently, it was exposed to UV-light with a dose of 15mJ/mm<sup>2</sup>. After the illumination process, the dish was thoroughly washed with milliQ water and rehydrated with PBS for 5min. Following rehydration, the dish was incubated with 20 $\mu\text{g}/\text{ml}$  of labeled Fibronectin-Alexa647 (provided by Y-proteins, ThermoFisher) for 15min at room temperature. Samples are stored in PBS at room temperature until cell seeding.

## Cell culture

MDA-MB-231 human breast carcinoma epithelial cells, co-expressing fluorescently labeled histones (mcherry-H2B), are cultured in common growth medium L-15 (Sigma) supplemented with 10% foetal bovine serum (Sigma). The cells are cultivated at a temperature of 37°C up to 80-90% confluence. Following this, the cells were washed and trypsinized for 4min. For experimental purposes, the cell solution is centrifuged at 1,000 r.c.f. for 3min. Subsequently, the cells were re-suspended in L-15. Approximately 8,000 cells were seeded per  $\mu$ -dish (ibidi), allowing them to adhere for a minimum duration of 3h.

## Microscopy and cell tracking

Measurements were performed in time-lapse mode for up to 48h on a Nikon-Eclipse TI-E inverted microscope. To provide standard incubation conditions throughout the measurements, the microscope is equipped with gas incubation and a heating system (Okolab). Bright-field and fluorescence images of the fibronectin-coated pattern and the co-expressed labeled histones were acquired every 10min. A bandpass filter is applied to the images of the nuclei to enhance their quality. Following this, the images were binarized, and the positions of the nuclei's center-of-mass were determined using the Analyze Particles plugin in ImageJ.

---

\* [c.p.broedersz@vu.nl](mailto:c.p.broedersz@vu.nl)

- [1] P. Sens, Stick-slip model for actin-driven cell protrusions, cell polarization, and crawling, [Proceedings of the National Academy of Sciences](#) **117**, 24670 (2020).
- [2] D. B. Brückner, M. Schmitt, A. Fink, G. Ladurner, J. Flommersfeld, N. Arlt, E. Hannezo, J. O. Rädler, and C. P. Broedersz, Geometry Adaptation of Protrusion and Polarity Dynamics in Confined Cell Migration, [Physical Review X](#) **12**, 031041 (2022).
- [3] E. A. Evans and D. A. Calderwood, Forces and Bond Dynamics in Cell Adhesion, [Science](#) **316**, 1148 (2007).
- [4] G. I. Bell, Models for the Specific Adhesion of Cells to Cells: A theoretical framework for adhesion mediated by reversible bonds between cell surface molecules., [Science](#) **200**, 618 (1978).
- [5] J. Damiano-Guercio, L. Kurzawa, J. Mueller, G. Dimchev, M. Schaks, M. Nemethova, T. Pokrant, S. Brühmann, J. Linkner, L. Blanchoin, M. Sixt, K. Rottner, and J. Faix, Loss of Ena/VASP interferes with lamellipodium architecture, motility and integrin-dependent adhesion, [eLife](#) **9**, e55351 (2020).
- [6] T. M. Svitkina, A. B. Verkhovskiy, K. M. McQuade, and G. G. Borisy, Analysis of the Actin-Myosin II System in Fish Epidermal Keratocytes: Mechanism of Cell Body Translocation, [Journal of Cell Biology](#) **139**, 397 (1997).